Contrast-Enhanced X-ray Detection of Microcalcifications in Radiographically Dense Mammary Tissue Using Targeted Gold Nanoparticles

Lisa E. Cole,[†,§] Tracy Vargo-Gogola,[‡,§] and Ryan K. Roeder[*,†,§]

[†]Department of Aerospace and Mechanical Engineering, Bioengineering Graduate Program and [§]Harper Cancer Research Institute, University of Notre Dame, Notre Dame, Indiana 46556, United States and [‡]Department of Biochemistry and Molecular Biology, Indiana University Simon Cancer Center, Indiana University School of Medicine — South Bend, South Bend, Indiana 46617, United States

ABSTRACT Breast density reduces the accuracy of mammography, motivating methods to improve sensitivity and specificity for detecting abnormalities within dense breast tissue, but preclinical animal models are lacking. Therefore, the objectives of this study were to investigate a murine model of radiographically dense mammary tissue and contrast-enhanced X-ray detection of microcalcifications in dense mammary tissue by targeted delivery of bisphosphonate-functionalized gold nanoparticles (BP-Au NPs). Mammary glands (MGs) in the mouse mammary tumor virus - polyomavirus middle T antigen (MMTV-PyMT or PyMT) model exhibited greater radiographic density with age and compared with strain- and age-matched wild-type (WT) controls at 6−10 weeks of age. The greater radiographic density of MGs in PyMT mice obscured radiographic detection of microcalcifications that were otherwise detectable in MGs of WT mice. However, BP-Au NPs provided enhanced contrast for the detection of microcalcifications in both radiographically dense (PyMT) and WT mammary tissues as measured by computed tomography after intramammary delivery. BP-Au NPs targeted microcalcifications to enhance X-ray contrast with surrounding mammary tissue, which resulted in improved sensitivity and specificity for detection in radiographically dense mammary tissues.

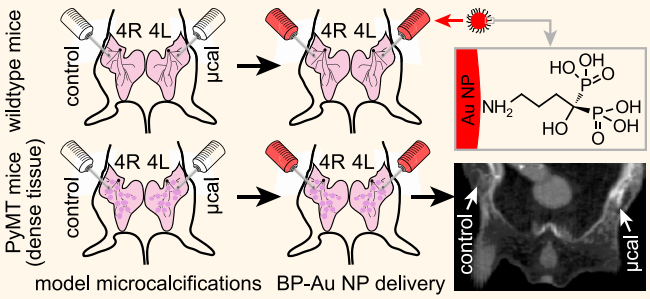

KEYWORDS: breast microcalcifications · contrast agent · mammographic density · gold nanoparticles · targeted delivery · X-ray imaging

Breast cancer is the most common cancer and the second leading cause of cancer-related deaths.[1] Early detection of breast abnormalities through mammographic screening has reduced breast cancer mortality[2,3] by enabling the initiation of treatment prior to disease progression. Mammography uses a low dose of X-rays to visualize breast tissue on a projected image to screen for atypical changes over time. Mammographic screening for breast cancer is an effective early detection platform with a sensitivity of 75% and specificity of 92.3% for the general population.[4] However, breast tissue density varies greatly among women, and the accuracy of mammography is dramatically decreased with increased breast density.[5,6]

Breast tissue density is observed radiographically by areas of high X-ray attenuation on a mammogram and histologically by a greater proportion of fibrous and glandular tissue relative to adipose tissue. Women with 75% of the breast composed of dense tissue have an estimated four- to six-fold increased risk of developing breast cancer.[7,8] Thus, women with elevated breast density are at greater risk for developing breast cancer, while mammography is less likely to provide accurate detection. For example, breast microcalcifications (μcals) are an important early marker for breast cancer that are commonly detected by mammography due to exhibiting a greater X-ray attenuation compared with low-density adipose tissue.[9] However, tissue exhibiting

* Address correspondence to rroeder@nd.edu.

Received for review May 7, 2015 and accepted August 26, 2015.

Published online August 26, 2015
10.1021/acsnano.5b02749

greater radiographic density can mask μcals causing these early atypical changes to be missed during mammographic screening.[10−12] Therefore, women with dense breast tissue are often screened with other imaging modalities as an adjunct to mammography.[13]

Ultrasound,[6,13] magnetic resonance imaging (MRI),[13] and molecular breast imaging (MBI)[14] have exhibited greater sensitivity compared with mammography for detecting abnormalities in women with increased breast density.[15] Unfortunately, these modalities each have limitations inhibiting widespread clinical adoption. Both ultrasound and MRI are limited by low specificity resulting in a high number of false positives,[15] which have been shown to increase patient anxiety[16] and healthcare costs[17] due to unnecessary biopsies. MRI is also limited by high costs compared with mammography.[18] MBI is limited by a relatively high radiation dose and low spatial resolution.[19] Thus, in this preclinical study we investigated the potential of using a targeted nanoparticle contrast agent to improve the radiographic detection of a breast tissue abnormality in both normal and radiographically dense mammary tissue.

X-ray contrast agents could be used to improve the sensitivity and specificity for detecting abnormalities in dense breast tissue using existing mammography instrumentation. Gold nanoparticles (Au NPs) have shown potential as an X-ray contrast agent due to exhibiting higher X-ray attenuation compared with iodine,[20−23] low cytotoxicity,[20,24,25] and facile surface functionalization for colloidal stability[20−22] and targeted delivery[20,26−29] *in vivo*. We recently demonstrated that bisphosphonate-functionalized Au NPs (BP-Au NPs) were able to target breast μcals and improve the sensitivity and specificity for detection by computed tomography (CT) in both *in vitro*[30] and *in vivo*[31] models. Targeted delivery was enabled by bisphosphonate ligands, which exhibit high binding affinity for hydroxyapatite (HA),[32] the mineral component of μcals associated with malignant breast lesions.[9] However, the mammary glands (MGs) of wild-type (WT) mice used in these studies exhibited low background intensity and variability, which is not representative of women with radiographically dense breast tissue.

Here we report the characterization of a murine model of human radiographic breast density and the use of this model to investigate contrast-enhanced X-ray detection of μcals in radiographically dense mammary tissue via targeted delivery of BP-Au NPs. An established transgenic mouse model of breast cancer, the mouse mammary tumor virus - polyomavirus middle T antigen (MMTV-PyMT or PyMT) model,[33] was investigated as a model of radiographically dense breast tissue, due to evidence of increased X-ray attenuation exhibited by MGs of PyMT mice compared with WT mice.[34] The μcals were created in the MGs of both WT and PyMT mice to determine if the increased background intensity of the MGs in PyMT mice affected the detection of μcals by X-ray imaging. Finally, these models were combined to investigate *in vivo* targeted delivery of BP-Au NPs and contrast-enhanced X-ray detection of μcals in radiographically dense mammary tissues.

RESULTS AND DISCUSSION

Murine Model of Radiographically Dense Mammary Tissue. WT and PyMT mice were imaged *in vivo* by planar radiography and CT at 6, 7, 8, 9, and 10 weeks of age (Figure 1). For radiography, the left number 4 (4L) MG was pulled away from the body cavity similar to a human mammogram.[34] WT mice exhibited low radiographic density, little variability within MGs, and no change with age (Figure 1a). In contrast, PyMT mice exhibited greater radiographic density, greater variability within MGs, and increased radiographic density with age (Figure 1a). Radiographic breast density was quantified by X-ray attenuation measurements in CT. The X-ray attenuation measured for PyMT mice increased with increasing age ($p < 0.01$, ANOVA), while WT mice exhibited no change with age ($p = 0.96$, ANOVA) (Figure 1b). PyMT mice exhibited significantly greater X-ray attenuation compared with WT mice at each age ($p < 0.05$, *t*-test), and these differences were readily apparent in reconstructed three-dimensional (3D) CT images (Figure 1b). Carmine alum whole mounts (Figure 1c) and Masson's trichrome staining (Figure 1d) confirmed that the increased radiographic density of PyMT compared with WT mice was due to the presence of optically opaque regions of hyperplastic epithelium and greater amounts of collagen in MGs.

The presence of radiographically dense breast tissue in humans is known to be due to a high percentage of fibroglandular tissue compared with adipose tissue. The fibroglandular and adipose components of human breast tissue were previously determined to exhibit an X-ray attenuation of approximately 20 and −260 HU, respectively, by CT at 45 kVp.[35,36] The X-ray attenuation exhibited by MGs in PyMT mice at 8−10 weeks of age was not statistically different from 20 HU ($p > 0.17$, exact *t*-test). Therefore, PyMT mice were able to recapitulate the X-ray attenuation associated with the fibroglandular component of human breast tissue, and PyMT mice at 7−8 weeks of age were subsequently used in this study to model radiographically dense breast tissue.

MMTV-PyMT mice are commonly used as a mammary tumor model with a well-characterized temporal progression.[37] A previous study used the PyMT model to investigate the effect of mammary tissue density on tumor development and progression,[38] but did not investigate the effect of tissue density on cancer detection or imaging. Hariri *et al*. observed that MGs in a PyMT mouse at 80 days of age exhibited increased

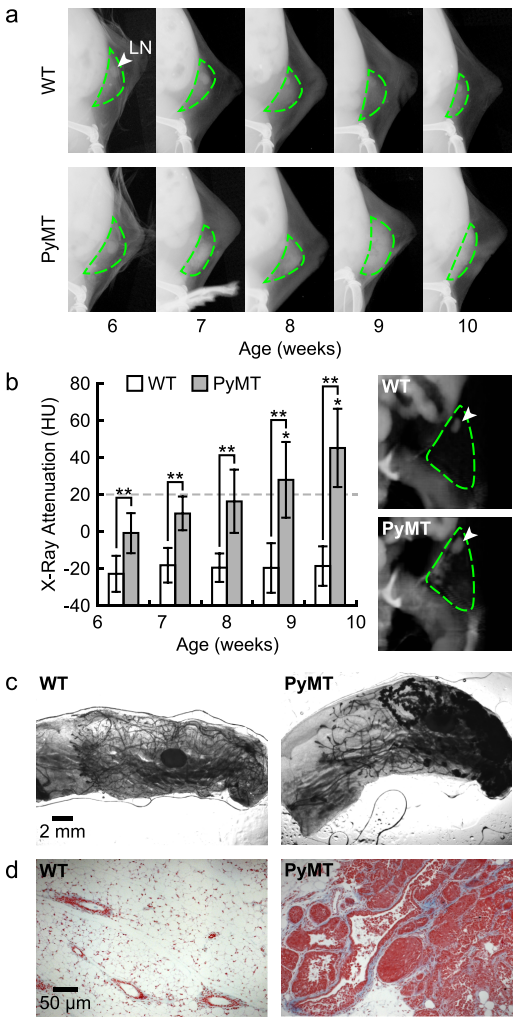

Figure 1. Characterization of a murine model of radiographically dense mammary tissue (PyMT) compared with WT mice at 6, 7, 8, 9, and 10 weeks of age showing (a) representative planar radiographs of 4L MGs (dashed outline), (b) the X-ray attenuation (HU) measured *in vivo* by CT for 4L MGs and representative reconstructed 3D CT images of 4L MGs (dashed outline) at 7 weeks of age, (c) representative carmine alum stained whole mounts of 4L MGs at 7 weeks of age, and (d) representative Masson's trichrome stained tissue sections of 4L MGs at 7 weeks of age showing an increased presence of collagen (blue) around the hyperplastic epithelial cells (red) of PyMT mice. White arrowheads point to the lymph node (LN), which was used as an anatomic landmark for the MG. Note that human glandular tissue exhibits an X-ray attenuation of 20 HU at 45 kVp, indicated by the dashed line in (b). Error bars show one standard deviation of the mean (n = 3−5/group). *p < 0.05 vs 6 weeks of age, t-test. **p < 0.05 WT vs PyMT, t-test.

radiographic density compared with WT controls using planar radiography.[34] However, this mouse also exhibited widespread tumor burden within MGs and the presence of palpable tumors, which is undesirable for investigating the effects of mammary tissue density independent of widespread and variable tumor burden. Therefore, we investigated PyMT mice at an earlier premalignant stage when the MG becomes hyperplastic with increased epithelial cell deposition at 4−7 weeks of age.[37] We demonstrated that the hyperplastic epithelium alone was sufficient for recapitulating the X-ray attenuation associated with human fibroglandular tissue[36] and thus serving as a premalignant murine model of breast density (Figure 1).

The main limitation of this murine model is that the radiographic density of MGs in PyMT mice is directly associated with the presence of premalignant hyperplastic epithelium. Hyperplasia does not recapitulate the biological phenotype of human radiographic density, which is associated with healthy fibroglandular tissue within the breast.[39,40] Thus, the premalignant PyMT model is an effective imaging model for radiographic density but is not suitable for investigating the effect of breast density on tumor development or progression. A murine model of breast density that does not require the formation of premalignant tissue would enable investigations in healthy dense tissues. Another important limitation of this murine model is that murine MGs are an order of magnitude thinner compared with human breast tissue and the signal-to-noise ratio is expected to decrease with increased tissue thickness. Therefore, other models, such as imaging phantoms and cadaveric tissue, will be required to evaluate the effects of radiographic density at a clinically relevant tissue thickness.

Murine Model of μcals Within Radiographically Dense Mammary Tissue. The murine model of radiographically dense mammary tissue was combined with a previously developed murine model of μcals.[31] HA crystals were mixed in a Matrigel carrier at varying concentrations (3.0, 5.0, and 10 mg/mL HA) and injected into the fat pad of the 4L MG in WT and PyMT mice at 7−8 weeks of age. Matrigel without HA was injected into the 4R MG as a contralateral control. X-ray attenuation was measured within a volume-of-interest (VOI) for the entire MG, including the lymph node (LN), areas of dense tissue, and HA μcals (Figure 2a). MGs containing 3.0 mg/mL HA μcals exhibited greater X-ray attenuation compared with controls in WT mice (p < 0.05, paired t-test) but not PyMT mice (p = 0.59, paired t-test) (Figure 2b). Thus, μcals containing 3.0 mg/mL HA were detectable in WT mice but not PyMT mice. MGs containing 5.0 (Figure 2c) and 10 (Figure 2d) mg/mL HA μcals exhibited greater X-ray attenuation compared with controls in both WT and PyMT mice (p < 0.05, paired t-test). Thus, μcals containing 5.0 and 10 mg/mL HA were detectable in both WT and PyMT mice. Importantly, μcals were visually apparent in grayscale planar radiographs for all HA levels in WT mice and for 10 mg/mL HA in PyMT mice, but the radiographic density of MGs in PyMT mice obscured the boundary of μcals containing 3.0 and 5.0 mg/mL HA from the surrounding dense tissue (Figure 2). Moreover, the X-ray attenuation of PyMT controls was not statistically different from μcals in WT mice at each HA level (p > 0.21, unpaired t-test).

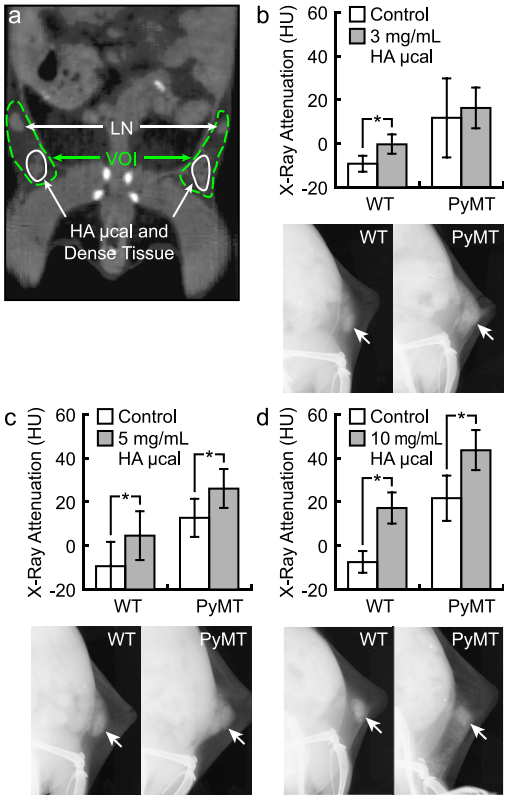

Figure 2. Characterization of a murine model of μcals within radiographically dense mammary tissue (PyMT) compared with WT mice. (a) Schematic diagram showing the VOI (dashed line) for the 4L and 4R MGs including μcals and Matrigel controls (solid line), respectively. The X-ray attenuation (HU) was measured *in vivo* by CT for MGs with μcals containing (b) 3.0, (c) 5.0, and (d) 10 mg/mL HA compared with Matrigel controls in WT and PyMT mice. Error bars show one standard deviation of the mean (n = 5/group). Representative planar radiographs of MGs in live mice show μcals (white arrows) within normal (WT) and radiographically dense (PyMT) tissues. See Figure 1a for representative planar radiographs of WT and PyMT controls. * $p < 0.05$, paired t-test.

The murine model of μcals within normal (WT) and radiographically dense (PyMT) mammary tissue was able to recapitulate the clinical challenges of detecting small abnormalities in dense breast tissue by X-ray imaging. The detection limit for μcals in radiographically dense mammary tissue (PyMT) was shown to be >3 mg/mL HA in this study. The detection limit for μcals in normal mammary tissues (WT) was previously shown to be >0.5 mg/mL HA using the same μcal model and imaging system.[31] Therefore, dense mammary tissue resulted in an approximately 6-fold decrease in sensitivity for the detection of μcals due to masking the presence of tissue abnormalities. Furthermore, the radiographic density of MGs in PyMT mice was indistinguishable from WT mice with μcals, and the same radiographic density obscured the distinction of μcals from surrounding dense tissue in PyMT mice, suggesting decreased specificity for the detection of μcals.

Matrigel injections without HA (control) had no effect on the X-ray attenuation of MGs in either WT or PyMT mice. Differences in the X-ray attenuation of MGs with (Figure 2) and without (Figure 1) the injected volume of Matrigel were not statistically significant for either WT ($p = 0.17$, t-test) or PyMT ($p = 0.65$, t-test) mice when analyzed using the same VOI. Note that the X-ray attenuation measurements reported in Figures 1 and 2 cannot be directly compared due to the use of a different VOI for each experiment, as detailed in the methods.

Two HA concentrations were chosen to mimic different levels of μcal burden for investigating contrast-enhanced detection of μcals within radiographically dense mammary tissue based on the preceding model characterization. The μcals containing 3.0 mg/mL HA were shown to be undetectable by CT in MGs of PyMT mice, but detectable in MGs of WT mice (Figure 2b), modeling a clinical situation (false negative) where breast tissue abnormalities are masked by dense breast tissue.[8] The μcals containing 5.0 mg/mL HA were detectable by CT in MGs of both PyMT and WT mice, but were difficult to distinguish from the surrounding dense tissue in PyMT mice, modeling a clinical situation (false positive) where radiographically dense tissues are mistaken as breast tissue abnormalities.[10]

Targeted Delivery of BP-Au NPs to μcals Within Radiographically Dense Mammary Tissue. BP-Au NPs were prepared for *in vivo* targeted delivery (Supporting Information Figure S1), as described previously.[31] Prior to *in vivo* administration, BP-Au NPs were characterized as monodispersed and spherical with a mean (±standard deviation) particle diameter of 12.5 (1.3) nm measured by transmission electron microscopy (TEM), a hydrodynamic diameter of 49.3 (1.6) nm measured by dynamic light scattering (DLS), and a characteristic surface plasmon resonance peak at ~527 nm in ultraviolet−visible (UV−vis) spectroscopy (Supporting Information). The hydrodynamic diameter, which accounts for the apparent size of the hydrated particle including associated ions and molecules, was larger than the physical diameter, as expected.[41] All results were consistent with previously published results for ~13 nm BP-Au NPs.[30−32,41,42] Additionally, the gold concentration was measured to be 50 mM by inductively coupled plasma-optical emission spectroscopy (ICP-OES). X-ray attenuation is not influenced by the size of the Au NPs at equal mass concentration;[42] therefore, Au NPs ~13 nm in diameter were used, as this size was previously shown to exhibit colloidal stability and high binding affinity to HA crystals *in vivo* using a similar μcal model in WT mice.[31]

The murine model of μcals within radiographically dense tissue was used to investigate targeted delivery of BP-Au NPs to μcals containing 3.0 or 5.0 mg/mL HA within the 4L MGs of WT (Figure 3a) and PyMT mice (Figure 3b). Matrigel without HA was injected into the 4R MGs as a contralateral control. After creating μcals, mice were imaged by CT prior to delivering BP-Au NPs

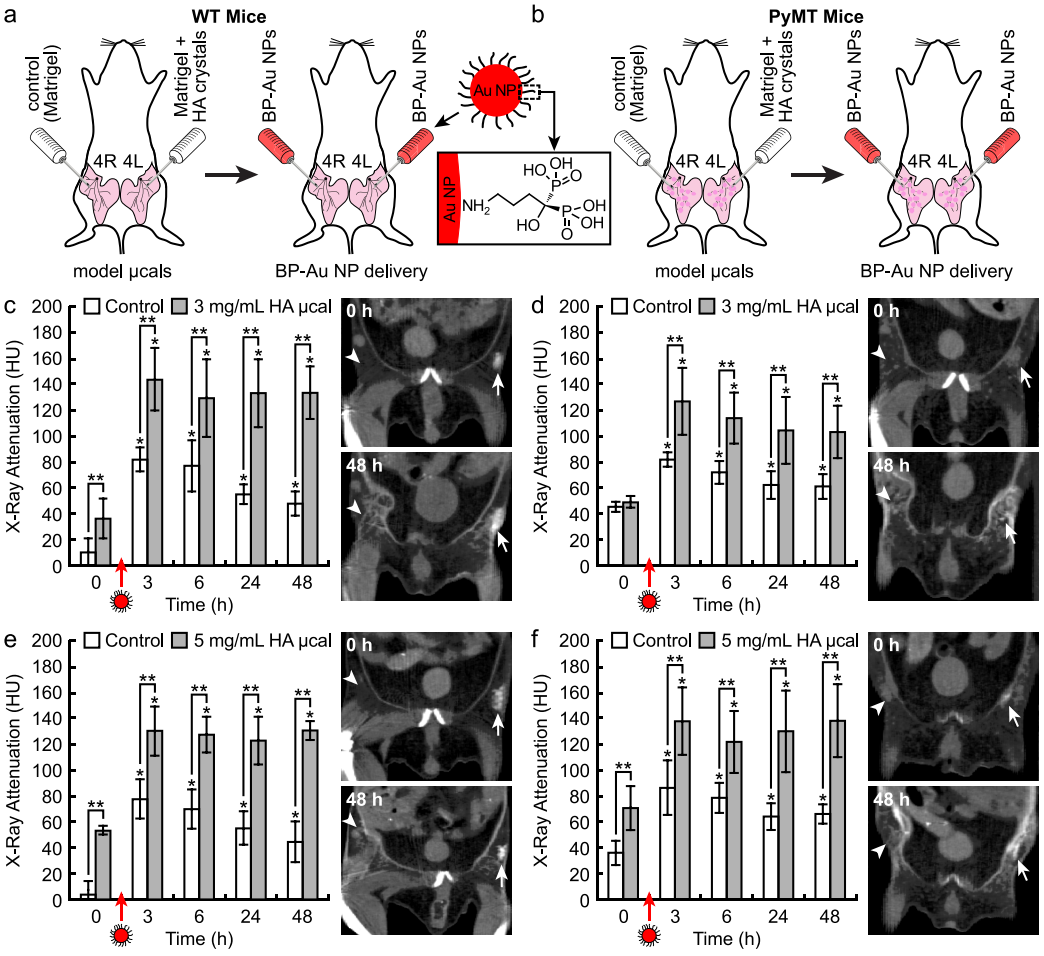

Figure 3. Targeted delivery of BP-Au NPs to μcals within (a) WT and (b) radiographically dense mammary tissue of MMTV-PyMT mice showing the experimental design and BP-Au NPs. The X-ray attenuation (HU) was measured *in vivo* by CT for μcals containing (c,d) 3.0 and (e,f) 5.0 mg/mL HA compared with contralateral Matrigel controls in (c,e) WT and (d,f) PyMT mice, before (0 h) and longitudinally at 3, 6, 24, and 48 h after delivering BP-Au NPs. Error bars show one standard deviation of the mean (n = 6/group). Representative 2D grayscale CT images for (c,e) WT and (d,f) PyMT mice showing μcals containing (c,d) 3.0 and (e,f) 5.0 mg/mL HA in 4L MGs (arrows), and contralateral Matrigel controls in 4R MGs (arrowheads), before (0 h) and 48 h after delivering BP-Au NPs. *p < 0.05 vs 0 h, t-test. **p < 0.05 μcal vs control, paired t-test.

(0 h) and longitudinally at 3, 6, 24, and 48 h after delivering BP-Au NPs via intramammary injection into both the 4L and 4R MGs (Figure 3).

Microcalcifications containing 3.0 mg/mL HA were investigated to model the effects of dense mammary tissue on the sensitivity of detection (Figure 3c,d). Prior to delivering BP-Au NPs (0 h), the X-ray attenuation exhibited by MGs with μcals was greater than Matrigel controls in WT mice (p < 0.01, paired t-test) (Figure 3c), but not PyMT mice (p = 0.10, paired t-test) (Figure 3d) due to tissue density masking the detection of μcals. After delivering BP-Au NPs, the X-ray attenuation of both MGs was increased at each time point for both WT (Figure 3c) and PyMT (Figure 3d) mice compared with before delivery (p < 0.001, t-test) and was significantly greater for MGs containing μcals compared with controls at each time point for both WT (Figure 3c) and PyMT (Figure 3d) mice (p < 0.05, paired t-test). The relative contrast enhancement of μcals targeted by BP-Au NPs compared with contralateral controls was visibly evident in two-dimensional (2D) grayscale CT images of MGs in both WT (Figure 3c) and PyMT mice (Figure 3d), and was quantified by the differential contrast (ΔHU) before (0 h) and 48 h after delivering Au NPs (Figure 4a). The increased tissue density of PyMT mice resulted in decreased ΔHU compared with WT mice both before and after delivery (p < 0.05, t-test). However, the delivery of BP-Au NPs significantly increased ΔHU compared with before delivery for both WT and PyMT mice (p < 0.005, paired t-test), such that μcals containing 3.0 mg/mL HA were detectable in PyMT mice (Figure 4a). Note that a differential contrast (ΔHU) of at least 30 HU[43,44] has been suggested to be necessary for visibly apparent enhanced-contrast in CT. Therefore, BP-Au NPs enabled improved sensitivity for the detection of μcals that were otherwise undetectable by X-ray imaging in radiographically dense mammary tissues.

Microcalcifications containing 5.0 mg/mL HA were investigated to model the effects of dense mammary

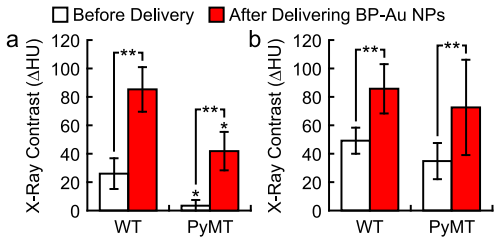

Figure 4. Differential contrast (ΔHU) measured by CT in radiographically dense mammary tissue (PyMT) compared with WT mice for MGs with μcals containing (a) 3.0 mg/mL and (b) 5.0 mg/mL HA before and 48 h after delivering BP-Au NPs. Error bars show one standard deviation of the mean (n = 6/group). *p < 0.05 WT vs PyMT, t-test. **p < 0.05 before vs after delivering BP-Au NPs, paired t-test.

tissue on detection specificity (Figure 3e, 3f). Prior to delivering BP-Au NPs (0 h), the X-ray attenuation exhibited by MGs with μcals was greater than Matrigel controls in both WT (Figure 3e) and PyMT (Figure 3f) mice (p < 0.01, paired t-test). After delivering BP-Au NPs, the X-ray attenuation of both MGs was increased at each time point for both WT (Figure 3e) and PyMT (Figure 3f) mice compared with before delivery (p < 0.001, t-test), and was significantly greater for MGs containing μcals compared with controls at each time point for both WT (Figure 3e) and PyMT (Figure 3f) mice (p < 0.05, paired t-test). The relative contrast enhancement of μcals targeted by BP-Au NPs compared with contralateral controls was visibly evident in 2D gray-scale CT images of MGs in both WT (Figure 3e) and PyMT (Figure 3f) mice and was quantified by ΔHU before (0 h) and 48 h after delivering Au NPs (Figure 4b). The increased tissue density of PyMT mice resulted in decreased ΔHU compared with WT mice before delivery (p = 0.05, t-test), but the difference after delivery was not statistically significant (p = 0.42, t-test). However, the delivery of BP-Au NPs significantly increased ΔHU compared with before delivery for both WT and PyMT mice (p < 0.05, paired t-test), such that a false positive could be ruled out (Figure 4b). Therefore, BP-Au NPs enabled improved specificity for the detection of μcals in radiographically dense mammary tissues.

The radiographic density of MGs in PyMT mice obscured the detection of μcals due to increased absorption or scattering of X-ray photons by the greater levels of fibroglandular tissue (Figure 2). However, targeted delivery of BP-Au NPs enhanced contrast to improve the sensitivity and specificity for detecting μcals that were previously undetectable and detectable, respectively, in both normal (WT) and radiographically dense mammary tissue (PyMT) (Figure 3). The levels of contrast enhancement that were achieved (Figure 4) were similar to other studies investigating functionalized Au NPs as X-ray contrast agents for tumor targeting[26,29,45] and our previous study for targeting μcals in normal murine MGs.[31] Therefore, the results of this study suggest that targeted X-ray contrast agents like BP-Au NPs have the potential to improve mammographic screening in radiographically dense breast tissue.

A limitation of this study is that μcals are only associated with breast cancer and may not be predictive of cancerous lesions.[9] Investigations aimed at improving the detection of small cancerous lesions within dense breast tissue would be highly advantageous, as the average size of tumors detected in dense breasts has been shown to be greater than in mostly fatty breast tissue.[13] Nonetheless, the results of this study demonstrated that a targeted nanoparticle contrast agent enabled improved sensitivity and specificity for the detection of a common tissue abnormality (μcals). Moreover, the ability to tailor the μcal burden *a priori* in this model may serve as a useful surrogate for small cancerous lesions when investigating the effect of masking on the detection of tissue abnormalities in dense breast tissue. However, possible differences in the efficiency of targeted delivery to μcals versus tumors are not known and must be considered. The use of intramammary delivery in this study almost certainly improved targeted delivery compared in intravenous delivery. Similarly, intratumoral delivery has been shown to improve targeted delivery and contrast enhancement compared to intravenous delivery.[45−47] While systemic delivery may be viewed as ideal, particularly for detecting unknown cancers, local delivery may be advantageous to ensure efficient delivery when screening for a specific cancer, like breast cancer. Finally, X-ray attenuation measurements suggested that BP-Au NPs were retained within MGs containing μcals, and gradually cleared from control MGs and tissue surrounding μcals after delivery, but the clearance of BP-Au NPs was not complete by the final study time point at 48 h (Figure 3). Therefore, the biodistribution of BP-Au NPs was investigated on excised tissues.

***In Vivo* Biodistribution of BP-Au NPs.** The mass of gold in various tissues was measured 48 h after delivering BP-Au NPs in WT and PyMT mice (Figure 5). The highest concentrations of gold were measured in the μcals, both the 3.0 (Figure 5a) and 5.0 mg/mL (Figure 5b) HA concentrations, and were at least 1 order of magnitude greater than gold concentrations measured in surrounding tissues and organs commonly involved in clearing nanoparticles (Figure 5). Therefore, BP-Au NPs were confirmed to target μcals due to a high binding affinity to HA crystals. Specific binding of BP-Au NPs to HA crystals within μcals was further verified by direct observation of BP-Au NPs bound to the surface of HA crystals within μcals dissected 48 h after delivering of BP-Au NPs (Figure 5c). The concentration of gold within the surrounding tissue of both the 4R (control) and 4L (μcal) MGs, as well as the adjacent peritoneum and skin, was significantly lower compared with μcals but significantly greater compared with the liver, spleen,

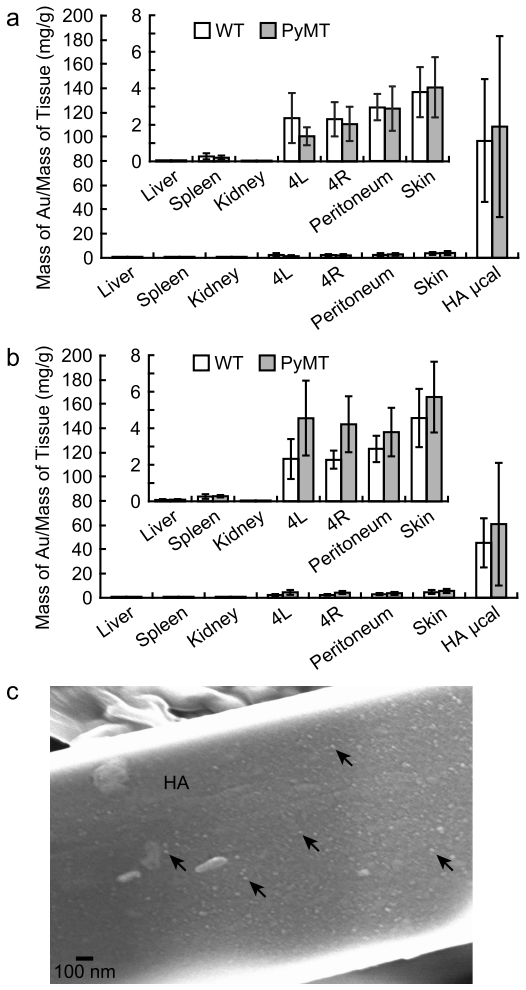

Figure 5. Biodistribution of gold in organs known to accumulate Au NPs, as well as MGs (4L, 4R) and targeted μcals, 48 h after delivering BP-Au NPs to WT and PyMT mice with μcals containing (a) 3.0 and (b) 5.0 mg/mL HA in the 4L MG. Error bars show one standard deviation of the mean (*n* = 6/group). (c) Representative scanning electron micrograph confirming specific binding of BP-Au NPs (arrows) to the surface of a HA crystal from within a μcal that was dissected 48 h after delivering BP-Au NPs in WT mice.

and kidneys (Figure 5). This result confirmed that BP-Au NPs were being cleared but were not yet completely cleared from the intramammary injection site. Differences in the concentration of gold detected in the tissues of WT versus PyMT mice were not statistically significant, indicating that the biodistribution was not affected by the mammary tissue density.

The mice did not exhibit any clinical signs of illness or discomfort during the 48 h observation period after delivering BP-Au NPs, similar to our previous study.[31] A rigorous assessment of cytotoxicity, longer term evaluation of clearance, and dosing studies will be necessary to continue toward clinical translation. Nonetheless, the results of this study are encouraging considering the significant contrast enhancement that was achieved with a relatively low administered dose of gold (2 mg/mouse or ~80 mg/kg) compared with previous studies.[20] This relatively low dose and the use of intramammary delivery also resulted in a low mass concentration of BP-Au NPs accumulated in the liver and spleen,[26,45−47] which are known to accumulate Au NPs after intravenous delivery.[22]

The key to achieving contrast enhancement in CT is to deliver a sufficiently large mass concentration of the contrast agent to the site of interest.[20] The biodistribution of BP-Au NPs indicated that the mass concentration of gold within μcals was in the range of 5−10 wt % (50−100 mg Au/g tissue) and that within the surrounding tissue of MGs was in the range of 0.1−0.5 wt % (Figure 5). We calculated the minimum detectable mass concentration of gold within highly mineralized tissue (bone) and breast tissue to be 0.17 and 0.07 wt %, respectively, at 45 keV and 0.34 and 0.27 wt %, respectively, at 80 keV, assuming that a differential contrast of 30 HU is necessary for detection.[48] A previous study similarly suggested that the minimum detectable mass concentration of gold in water was 5.8 mM or 0.11 wt %.[44] Therefore, the targeted delivery of BP-Au NPs to μcals in mammary tissue achieved a mass concentration of gold that was an order of magnitude greater than the minimum required for contrast enhancement. This result suggests that contrast enhancement is feasible at an even lower dose of gold than that used in this study and provides support for further investigation of BP-Au NPs and other targeted nanoparticle contrast agents for diagnostic X-ray imaging.

CONCLUSIONS

Murine models of mammary tissue density and μcals were developed and combined for investigating radiographic detection of abnormalities in radiographically dense breast tissue. MGs in PyMT mice exhibited greater radiographic density with age and compared with strain- and age-matched WT controls at 6−10 weeks of age. PyMT mice at 7−8 weeks of age were able to recapitulate the X-ray attenuation associated with the fibroglandular component of human breast tissue and were subsequently used to model radiographically dense breast tissue. The greater radiographic density of MGs in PyMT mice obscured radiographic detection of μcals that were otherwise detectable in MGs of WT mice. Therefore, the murine model of μcals within radiographically dense mammary tissue was able to recapitulate the clinical challenges of detecting small abnormalities in dense breast tissue by X-ray imaging. The targeted delivery of BP-Au NPs enabled improved sensitivity and specificity for the radiographic detection of μcals that were previously undetectable and detectable, respectively, in radiographically dense mammary tissues after intramammary delivery. Biodistribution data confirmed efficient targeting of BP-Au NPs to μcals, gradual clearance from the injection site, and low levels of uptake in the liver, spleen, and kidneys.

Therefore, the results of this study suggest that targeted X-ray contrast agents like BP-Au NPs have the potential to improve mammographic screening in radiographically dense breast tissue.

METHODS

Murine Model of Radiographically Dense Mammary Tissue. Female mice positive for the mouse mammary tumor virus - polyomavirus middle T antigen (MMTV-PyMT or PyMT) and wild-type (WT) mice were obtained by breeding male PyMT mice (Jackson Laboratory) on a FVB/NJ background with FVB females (Jackson Laboratory) lacking the PyMT transgene. This breeding generated females positive (PyMT) and negative (WT) for the PyMT transgene. All mice were genotyped for the PyMT transgene using polymerase chain reaction with DNA extracted from ear biopsies at 3 weeks of age. All procedures were approved by the Institutional Animal Care and Use Committee at the University of Notre Dame and were conducted in accordance with the guidelines of the U.S. Public Health Service Policy for Humane Care and Use of Laboratory Animals.

Female WT and PyMT mice were imaged *in vivo* by computed tomography (CT, Albira, Bruker) and planar radiography (In Vivo Xtreme, Bruker) at 6, 7, 8, 9, and 10 weeks of age (n = 3−5/group), using methods described below. Immediately after imaging, mice were sacrificed and left number 4 (4L) MGs were dissected and prepared for histology. Freshly dissected 4L MGs from WT and PyMT mice at 6, 7, 8, 9, and 10 weeks of age were fixed in 4% paraformaldehyde (PFA), rinsed in phosphate buffered saline and stained in carmine alum solution overnight at 25 °C with gentle mixing. After staining, MGs were rinsed and stored in 70% ethanol. Freshly dissected 4L MGs from WT and PyMT mice at 7 weeks of age were fixed in 4% PFA, embedded in paraffin, sectioned to 5 μm, and stained by Masson's trichrome (HT15-1KT, Sigma).

Murine Model of Microcalcifications Within Radiographically Dense Mammary Tissue. Microcalcifications were created within normal and radiographically dense mammary tissue in female WT and PyMT mice, respectively, at 7−8 weeks of age by injecting the 4L MG of anesthetized mice with 50 μL Matrigel (BD Biosciences) containing HA crystals[30,31] at concentrations of 3.0, 5.0, and 10 mg/mL HA (n = 5/group). Whisker-shaped HA crystals, exhibiting a mean length and width of ∼18 and ∼2 μm, respectively, were synthesized and characterized as described previously.[49] Matrigel alone was injected into the 4R MG as a contralateral control. Anesthetized mice were imaged *in vivo* by CT and planar radiography 24 h after creating μcals, using methods described below. Immediately after imaging, mice were sacrificed, and the 4L and 4R MGs were dissected and imaged with planar radiography, using methods described below.

Preparation and Characterization of BP-Au NPs. The synthesis and characterization of BP-Au NPs has been previously reported in detail.[32] Briefly, Au NPs were synthesized with a mean particle diameter of ∼13 nm and gold concentration of ∼0.5 mM using the citrate reduction method. As-synthesized Au NPs were surface functionalized with alendronate, which provided a primary amine for binding gold opposite a bisphosphonate (BP) functional group for targeting calcium in μcals. BP-Au NPs were concentrated to ∼50 mM (∼9.8 mg/mL) prior to administration *in vivo*.[31] Concentrated BP-Au NP solutions were characterized using standard techniques,[31] including ICP-OES for the concentration, TEM for the particle size, DLS for the hydrodynamic particle diameter, and UV−vis spectroscopy for colloidal stability.

Targeted Delivery of BP-Au NPs. HA μcals comprising 3.0 and 5.0 mg/mL HA were created in the 4L MG of WT and PyMT mice (n = 6/HA concentration/group), while the 4R MG was injected with Matrigel alone as a contralateral control, as described above. BP-Au NPs (50 mM) were administered to anesthetized mice 24 h after creating μcals by intramammary injection of a 100 μL dose (2 mg Au per mouse) into both the 4L and 4R MG. Mice were imaged *in vivo* by CT immediately prior to delivering BP-Au NPs (0 h) and longitudinally at 3, 6, 24, and 48 h after delivering BP-Au NPs, using methods described below. Mice were sacrificed immediately after imaging at 48 h. The liver, spleen, kidney, 4L and 4R MGs were dissected as well as the skin and peritoneum around each injection site. Microcalcifications were also subsequently dissected from the 4L MGs and analyzed separately. Tissues were dried overnight in an oven at 37 °C, massed, and digested in aqua regia (3 HCl:1 HNO_3) for 24 h. The mass of gold in each sample and mass of calcium in μcal samples were measured using ICP-OES (Optima 8000, PerkinElmer). Calibration curves were created by diluting certified standard gold and calcium solutions (SPEX CertiPrep).

Specific binding of BP-Au NPs to HA crystals in μcals was verified by scanning electron microsopy (SEM). A μcal containing 5 mg/mL HA was dissected from a WT mouse 48 h after delivering BP-Au NPs and incubated in 1.0 mg/mL collagenase (*Clostridium histolyticum* Type IA, Sigma) in phosphate buffered saline for 7 h at 37 °C to digest the extracellular matrix and expose HA crystals. HA crystals were removed from the solution, dried at 37 °C, mixed in 90% ethanol, pipetted onto a heated SEM sample holder, and coated with 2.5 nm iridium by sputter deposition. The sample was imaged using a field emission SEM (400 XHR, FEI, Hillsboro, OR) at an accelerating voltage of 5.0 kV and current of 6.3 pA.

***In Vivo* CT and Radiography.** Mice were imaged by CT (Albira, Bruker) at 45 kVp and 400 μA for 600 slices with a 250 ms integration time, 125 μm voxel size, and a 0.5 mm aluminum filter. The murine models for radiographically dense tissue and μcals were characterized by measuring the X-ray attenuation (HU) within a volume-of-interest (VOI) that encompassed the entire MG, including the lymph node, adipose tissue, fibroglandular tissue, and HA μcals (Figure 2a). The pooled mean (±standard deviation) VOI for the dense tissue and μcal models was 37.9 (4.6) mm^3. For the *in vivo* targeted delivery experiments, X-ray attenuation was measured within an animal-specific VOI determined by contrast between radiographically dense mammary tissue and surrounding adipose tissue prior to delivering BP-Au NPs and subsequently mapped onto CT images acquired longitudinally after delivering BP-Au NPs. The pooled mean (±standard deviation) VOI for this analysis was 14.3 (0.92) mm^3. The differential contrast (ΔHU) was calculated based on X-ray attenuation measurements before (0 h) and 48 h after delivering BP-Au NPs. ΔHU was measured as the difference in X-ray attenuation exhibited by MGs containing HA μcals and contralateral Matrigel controls. Mice and dissected MGs were also imaged by planar radiography (In Vivo Xtreme, Bruker) at 20 kVp with a 0.1 mm aluminum filter and 10 s exposure time. For *in vivo* radiography, the skin and 4L MG were pulled away from the body cavity and fixed to the specimen plate by tape to model a human mammogram.

Statistical Methods. All measurements were reported as the mean ± standard deviation. Differences in X-ray attenuation between WT and PyMT mice at each time point were examined using two-way analysis of variance (ANOVA, JMP 11, SAS Institute Inc.), and *post hoc* comparisons were performed using unpaired Student's t-tests. Differences between the X-ray attenuation of PyMT MGs at each time point and 20 HU were examined using an exact t-test. Differences in X-ray attenuation between μcals and Matrigel controls within WT and PyMT mice both before and after delivering BP-Au NPs were examined using paired t-tests. Changes in X-ray attenuation before and longitudinally after delivering BP-Au NPs for the μcal or Matrigel control within WT and PyMT mice were examined using one-way ANOVA, and *post hoc* comparisons were performed using paired t-tests. Differences in ΔHU were examined using two-way ANOVA; *post hoc* comparisons between WT and PyMT mice were performed using unpaired Student's t-tests; and *post hoc* comparisons before (0 h) and 48 h after delivering BP-Au NPs were performed using paired t-tests. The level of significance for all tests was set at $p < 0.05$.

Conflict of Interest: The authors declare no competing financial interest.

Supporting Information Available: The Supporting Information is available free of charge on the ACS Publications website at DOI: 10.1021/acsnano.5b02749.

Figure outlining characterization of BP-Au NPs (PDF)

Acknowledgment. This work was supported by a Seeding Research in Cancer (SRC) Grant from the St. Joseph Regional Medical Center in Mishawaka, IN, and an Engineering Novel Solutions to Cancer's Challenges at the Interdisciplinary Interface (ENSCCII) Training Grant from the Walther Cancer Foundation. This work was also partially supported by the National Science Foundation (DMR-1309587). The authors acknowledge the Freimann Life Science Center at the University of Notre Dame for the care of animals, the Notre Dame Integrated Imaging Facility for the use of CT and radiography, and the Center for Environmental Science and Technology at the University of Notre Dame for use of the ICP-OES.

REFERENCES AND NOTES

1. Siegel, R.; Ma, J.; Zou, Z.; Jemal, A. Cancer Statistics, 2014. *Ca-Cancer J. Clin.* **2014**, *64*, 9–29.
2. Smith, R. A.; Duffy, S. W.; Tabar, L. Breast Cancer Screening: the Evolving Evidence. *Oncology* **2012**, *26*, 471–486.
3. Tabar, L.; Vitak, B.; Chen, T. H.-H.; Yen, A. M.-F.; Cohen, A.; Tot, T.; Chiu, S. Y.-H.; Chen, S. L.-S.; Fann, J. C.-Y.; Rosell, J.; et al. Swedish Two-County Trial: Impact of Mammographic Screening on Breast Cancer Mortality During Three Decades. *Radiology* **2011**, *260*, 658–663.
4. Carney, P. A.; Miglioretti, D. L.; Yankaskas, B. C.; Kerlikowske, K.; Rosenberg, R.; Rutter, C. M.; Geller, B. M.; Abraham, L. A.; Taplin, S. H.; Dignan, M. Individual and Combined Effects of Age, Breast Density, and Hormone Replacement Therapy Use on the Accuracy of Screening Mammography. *Ann. Intern. Med.* **2003**, *138*, 168–175.
5. Kolb, T. M.; Lichy, J.; Newhouse, J. H. Comparison of the Performance of Screening Mammography, Physical Examination, and Breast US and Evaluation of Factors That Influence Them: an Analysis of 27,825 Patient Evaluations. *Radiology* **2002**, *225*, 165–175.
6. Britton, P.; Warwick, J.; Wallis, M. G.; O'Keeffe, S.; Taylor, K.; Sinnatamby, R.; Barter, S.; Gaskarth, M.; Duffy, S. W.; Wishart, G. C. Measuring the Accuracy of Diagnostic Imaging in Symptomatic Breast Patients: Team and Individual Performance. *Br. J. Radiol.* **2012**, *85*, 415–422.
7. Wolfe, J. N. Breast Patterns as an Index of Risk for Developing Breast Cancer. *AJR, Am. J. Roentgenol.* **1976**, *126*, 1130–1137.
8. Boyd, N. F.; Martin, L. J.; Yaffe, M. J.; Minkin, S. Mammographic Density and Breast Cancer Risk: Current Understanding and Future Prospects. *Breast Cancer Res.* **2011**, *13*, 1–12.
9. Morgan, M. P.; Cooke, M. M.; McCarthy, G. M. Microcalcifications Associated with Breast Cancer: an Epiphenomenon or Biologically Significant Feature of Selected Tumors? *J. Mammary Gland Biol. Neoplasia* **2005**, *10*, 181–187.
10. Cheng, H. D.; Cai, X.; Chen, X.; Hu, L.; Lou, X. Computer-Aided Detection and Classification of Microcalcifications in Mammograms: A Survey. *Pattern Recognit.* **2003**, *36*, 2967–2991.
11. Michell, M. J.; Iqbal, A.; Wasan, R. K.; Evans, D. R.; Peacock, C.; Lawinski, C. P.; Douiri, A.; Wilson, R.; Whelehan, P. A Comparison of the Accuracy of Film-Screen Mammography, Full-Field Digital Mammography, and Digital Breast Tomosynthesis. *Clin. Radiol.* **2012**, *67*, 976–981.
12. Tsai, C.-J.; Chen, R.-C.; Peng, H.-L.; Hsu, W.-L.; Lee, J. J. S. Improved Microcalcification Visualization using Dual-Energy Digital Mammography. *Acta Radiol.* **2013**, *54*, 614–621.
13. Al Mousa, D. S.; Ryan, E. A.; Mello-Thoms, C.; Brennan, P. C. What Effect Does Mammographic Breast Density Have on Lesion Detection in Digital Mammography? *Clin. Radiol.* **2014**, *69*, 333–341.
14. O'Connor, M.; Rhodes, D.; Hruska, C. Molecular Breast Imaging. *Expert Rev. Anticancer Ther.* **2009**, *9*, 1073–1080.
15. Drukteinis, J. S.; Mooney, B. P.; Flowers, C. I.; Gatenby, R. A. Beyond Mammography: New Frontiers in Breast Cancer Screening. *Am. J. Med.* **2013**, *126*, 472–479.
16. Brodersen, J.; Siersma, V. D. Long-Term Psychosocial Consequences of False-Positive Screening Mammography. *Ann. Family Med.* **2013**, *11*, 106–115.
17. Chubak, J.; Boudreau, D. M.; Fishman, P. A.; Elmore, J. G. Cost of Breast-Related Care in the Year Following False Positive Screening Mammograms. *Med. Care* **2010**, *48*, 815–820.
18. Fass, L. Imaging and Cancer: A Review. *Mol. Oncol.* **2008**, *2*, 115–152.
19. Specht, J. M.; Mankoff, D. A. Advances in Molecular Imaging for Breast Cancer Detection and Characterization. *Breast Cancer Res.* **2012**, *14*, 206.
20. Cole, L. E.; Ross, R. D.; Tilley, J. M.; Vargo-Gogola, T.; Roeder, R. K. Gold Nanoparticles as Contrast Agents in X-Ray Imaging and Computed Tomography. *Nanomedicine (London, U. K.)* **2015**, *10*, 321–341.
21. Cai, Q.-Y.; Kim, S. H.; Choi, K. S.; Kim, S. Y.; Byun, S. J.; Kim, K. W.; Park, S. H.; Juhng, S. K.; Yoon, K.-H. Colloidal Gold Nanoparticles as a Blood-Pool Contrast Agent for X-Ray Computed Tomography in Mice. *Invest. Radiol.* **2007**, *42*, 797–806.
22. Kim, D.; Park, S.; Lee, J. H.; Jeong, Y. Y.; Jon, S. Antibiofouling Polymer-Coated Gold Nanoparticles as a Contrast Agent for *in Vivo* X-Ray Computed Tomography Imaging. *J. Am. Chem. Soc.* **2007**, *129*, 7661–7665.
23. Hainfeld, J. F.; Slatkin, D. N.; Focella, T. M.; Smilowitz, H. M. Gold Nanoparticles: a New X-Ray Contrast Agent. *Br. J. Radiol.* **2006**, *79*, 248–253.
24. Khlebtsov, N.; Dykman, L. Biodistribution and Toxicity of Engineered Gold Nanoparticles: a Review of *in Vitro* and *in Vivo* Studies. *Chem. Soc. Rev.* **2011**, *40*, 1647–1671.
25. Alkilany, A. M.; Murphy, C. J. Toxicity and Cellular Uptake of Gold Nanoparticles: What We Have Learned So Far? *J. Nanopart. Res.* **2010**, *12*, 2313–2333.
26. Chanda, N.; Kattumuri, V.; Shukla, R.; Zambre, A.; Katti, K.; Upendran, A.; Kulkarni, R. R.; Kan, P.; Fent, G. M.; Casteel, S. W.; et al. Bombesin Functionalized Gold Nanoparticles Show *in Vitro* and *in Vivo* Cancer Receptor Specificity. *Proc. Natl. Acad. Sci. U. S. A.* **2010**, *107*, 8760–8765.
27. Eck, W.; Nicholson, A. I.; Zentgraf, H.; Semmler, W.; Bartling, S. Anti-CD4-Targeted Gold Nanoparticles Induce Specific Contrast Enhancement of Peripheral Lymph Nodes in X-Ray Computed Tomography of Live Mice. *Nano Lett.* **2010**, *10*, 2318–2322.
28. Hainfeld, J. F.; O'Connor, M. J.; Dilmanian, F. A.; Slatkin, D. N.; Adams, D. J.; Smilowitz, H. M. Micro-CT Enables Microlocalisation and Quantification of Her2-Targeted Gold Nanoparticles Within Tumour Regions. *Br. J. Radiol.* **2011**, *84*, 526–533.
29. Reuveni, T.; Motiei, M.; Romman, Z.; Popovtzer, A.; Popovtzer, R. Targeted Gold Nanoparticles Enable Molecular CT Imaging of Cancer: an *in Vivo* Study. *Int. J. Nanomed.* **2011**, *6*, 2859–2864.
30. Cole, L. E.; Vargo-Gogola, T.; Roeder, R. K. Bisphosphonate-Functionalized Gold Nanoparticles for Contrast-Enhanced X-Ray Detection of Breast Microcalcifications. *Biomaterials* **2014**, *35*, 2312–2321.
31. Cole, L. E.; Vargo-Gogola, T.; Roeder, R. K. Contrast-Enhanced X-Ray Detection of Breast Microcalcifications in a Murine Model Using Targeted Gold Nanoparticles. *ACS Nano* **2014**, *8*, 7486–7496.
32. Ross, R. D.; Roeder, R. K. Binding Affinity of Surface Functionalized Gold Nanoparticles to Hydroxyapatite. *J. Biomed. Mater. Res., Part A* **2011**, *99A*, 58–66.
33. Guy, C. T.; Cardiff, R. D.; Muller, W. J. Induction of Mammary Tumors by Expression of Polyomavirus Middle T Oncogene: a Transgenic Mouse Model for Metastatic Disease. *Mol. Cell. Biol.* **1992**, *12*, 954–961.
34. Hariri, M.; Wood, G. A.; DiGrappa, M. A.; MacPherson, M.; Backman, S. A.; Yaffe, M. J.; Mak, T. W.; Boyd, N. F.; Khokha, R.

Experimental Manipulation of Radiographic Density in Mouse Mammary Gland. *Breast Cancer Res.* **2004**, *6*, R540.
35. Johns, P. C.; Yaffe, M. J. X-Ray Characterisation of Normal and Neoplastic Breast Tissues. *Phys. Med. Biol.* **1987**, *32*, 675–695.
36. Boone, J. M.; Nelson, T. R.; Lindfors, K. K.; Seibert, J. A. Dedicated Breast CT: Radiation Dose and Image Quality Evaluation. *Radiology* **2001**, *221*, 657–667.
37. Lin, E. Y.; Jones, J. G.; Li, P.; Zhu, L.; Whitney, K. D.; Muller, W. J.; Pollard, J. W. Progression to Malignancy in the Polyoma Middle T Oncoprotein Mouse Breast Cancer Model Provides a Reliable Model for Human Diseases. *Am. J. Pathol.* **2003**, *163*, 2113–2126.
38. Provenzano, P. P.; Inman, D. R.; Eliceiri, K. W.; Knittel, J. G.; Yan, L.; Rueden, C. T.; White, J. G.; Keely, P. J. Collagen Density Promotes Mammary Tumor Initiation and Progression. *BMC Med.* **2008**, *6*, 11.
39. Hawes, D.; Downey, S.; Pearce, C.; Bartow, S.; Wan, P.; Pike, M. C.; Wu, A. H. Dense Breast Stromal Tissue Shows Greatly Increased Concentration of Breast Epithelium but No Increase in Its Proliferative Activity. *Breast Cancer Res.* **2006**, *8*, R24.
40. Boyd, N. F.; Martin, L. J.; Bronskill, M.; Yaffe, M. J.; Duric, N.; Minkin, S. Breast Tissue Composition and Susceptibility to Breast Cancer. *J. Natl. Cancer Inst.* **2010**, *102*, 1224–1237.
41. Ross, R. D.; Cole, L. E.; Roeder, R. K. Relative Binding Affinity of Carboxylate-, Phosphonate-, and Bisphosphonate-Functionalized Gold Nanoparticles Targeted to Damaged Bone Tissue. *J. Nanopart. Res.* **2012**, *14*, 1175.
42. Ross, R. D.; Cole, L. E.; Tilley, J. M. R.; Roeder, R. K. Effects of Functionalized Gold Nanoparticle Size on X-Ray Attenuation and Substrate Binding Affinity. *Chem. Mater.* **2014**, *26*, 1187–1194.
43. Krause, W. Delivery of Diagnostic Agents in Computed Tomography. *Adv. Drug Delivery Rev.* **1999**, *37*, 159–173.
44. Galper, M. W.; Saung, M. T.; Fuster, V.; Roessl, E.; Thran, A.; Proksa, R.; Fayad, Z. A.; Cormode, D. P. Effect of Computed Tomography Scanning Parameters on Gold Nanoparticle and Iodine Contrast. *Invest. Radiol.* **2012**, *47*, 475–481.
45. Wang, H.; Zheng, L.; Peng, C.; Shen, M.; Shi, X.; Zhang, G. Folic Acid-Modified Dendrimer-Entrapped Gold Nanoparticles as Nanoprobes for Targeted CT Imaging of Human Lung Adencarcinoma. *Biomaterials* **2013**, *34*, 470–480.
46. Yao, L.; Daniels, J.; Moshnikova, A.; Kuznetsov, S.; Ahmed, A.; Engelman, D. M.; Reshetnyak, Y. K.; Andreev, O. A. pHLIP Peptide Targets Nanogold Particles to Tumors. *Proc. Natl. Acad. Sci. U. S. A.* **2013**, *110*, 465–470.
47. Chattopadhyay, N.; Fonge, H.; Cai, Z.; Scollard, D.; Lechtman, E.; Done, S. J.; Pignol, J.-P.; Reilly, R. M. Role of Antibody-Mediated Tumor Targeting and Route of Administration in Nanoparticle Tumor Accumulation *in Vivo*. *Mol. Pharmaceutics* **2012**, *9*, 2168–2179.
48. Kouris, K.; Spyrou, N. M.; jackson, D. F. Minimum Detectable Quantities of Elements and Compounds in a Biological Matrix. *Nucl. Instrum. Methods Phys. Res.* **1981**, *187*, 539–545.
49. Roeder, R. K.; Converse, G. L.; Leng, H.; Yue, W. Kinetic Effects on Hydroxyapatite Whiskers Synthesized by the Chelate Decomposition Method. *J. Am. Ceram. Soc.* **2006**, *89*, 2096–2104.